Weighing nanoparticles in solution at the attogram scale

Selim Olcum[a,b,1], Nathan Cermak[c,1], Steven C. Wasserman[a], Kathleen S. Christine[d,e], Hiroshi Atsumi[f], Kris R. Payer[g], Wenjiang Shen[h], Jungchul Lee[i], Angela M. Belcher[a,b,f], Sangeeta N. Bhatia[b,d,e,j,k], and Scott R. Manalis[a,b,c,l,2]

Departments of [a]Biological Engineering, [f]Materials Science and Engineering, [j]Electrical Engineering and Computer Science, and [l]Mechanical Engineering, [b]Koch Institute for Integrative Cancer Research, [c]Computational and Systems Biology Initiative, [d]Harvard–MIT Health Sciences and Technology, [e]Institute for Medical Engineering and Science, and [g]Microsystems Technology Laboratories, Massachusetts Institute of Technology, Cambridge, MA 02139; [h]Innovative Micro Technology, Santa Barbara, CA 93117; [i]Department of Mechanical Engineering, Sogang University, Seoul 121-742, Korea; and [k]Howard Hughes Medical Institute, Cambridge, MA 02139

Physical characterization of nanoparticles is required for a wide range of applications. Nanomechanical resonators can quantify the mass of individual particles with detection limits down to a single atom in vacuum. However, applications are limited because performance is severely degraded in solution. Suspended micro- and nanochannel resonators have opened up the possibility of achieving vacuum-level precision for samples in the aqueous environment and a noise equivalent mass resolution of 27 attograms in 1-kHz bandwidth was previously achieved by Lee et al. [(2010) *Nano Lett* 10(7):2537–2542]. Here, we report on a series of advancements that have improved the resolution by more than 30-fold, to 0.85 attograms in the same bandwidth, approaching the thermomechanical noise limit and enabling precise quantification of particles down to 10 nm with a throughput of more than 18,000 particles per hour. We demonstrate the potential of this capability by comparing the mass distributions of exosomes produced by different cell types and by characterizing the yield of self-assembled DNA nanoparticle structures.

nanoparticle characterization | NEMS | microfluidics | mechanical oscillators

Many aspects of engineered and naturally occurring aqueous nanoparticles with diameters below 50 nm remain unexplored. Particles in this size range play a central role in a wide range of applications, including targeted drug delivery (1, 2), therapeutic protein formulation (3, 4), and the study of intracellular signaling via exosomes (5). In all these cases, function is strongly correlated to particle size and concentration. Established methods for characterizing these particles such as electron microscopy, dynamic light scattering (DLS), and disk centrifugation can determine the size of particles down to the nanometer scale, but generally have limitations when it comes to heterogeneous samples, throughput, measuring concentration, or ease of use (6–8). Miniaturized resistive pulse sensors (9, 10) can quantify size, heterogeneity, and concentration of particles bigger than about 50 nm, but require high salinity, which is an important consideration when characterizing biological nanoparticles, such as protein aggregates.

Nanomechanical resonators in vacuum can characterize nanoparticles down to a single atom (11, 12) or protein (13, 14), but perform poorly when immersed in solution. Resonators with embedded fluidic channels, known as suspended micro- and nanochannel resonators (15–17) (SMRs and SNRs), exploit the extreme sensitivity of measurement in vacuum, while measuring particles in solution. Although performance of nanomechanical resonators in vacuum has been studied extensively (11, 12, 18–20), the practical detection limits of SNRs have only received theoretical treatment to date (21). A proof-of-concept SNR implementation detected gold nanoparticles with a buoyant mass of 77 attograms (ag) at low throughput (bandwidth) (17), far above the thermomechanical noise limit and insufficient to detect lighter particles of biological interest, such as exosomes. The performance achieved here approaches the thermomechanical

noise limit, allowing us to measure the mass distributions of 10-nm gold particles and exosomes, which range in size from 30 to 100 nm (22).

Device Design and Evaluation

SNR systems work by measuring the resonant frequency of a microcantilever suspended in vacuum, which is extremely sensitive to changes in mass. A feedback loop keeps the cantilever oscillating at its resonant frequency while particles in solution flow through a U-shaped microfluidic channel running the length of the cantilever. As a particle passes through the cantilever, the cantilever mass transiently changes by the particle's buoyant mass (particle mass minus mass of the fluid it displaces), inducing a brief detectable change in the oscillation frequency. Thus, the signal magnitude depends on the difference between the fluid density and the particle density, but all other solvent properties, such as salinity, can be varied depending upon the desired sample environment.

Improving SNRs to achieve attogram-scale resolution with this method requires increasing mass sensitivity and reducing frequency noise. Mass sensitivity is proportional to the resonant frequency of the cantilever and inversely proportional to its mass (23), so we designed and fabricated a family of SNRs with reduced masses and increased resonant frequencies (Table 1). The mass of the smallest cantilever design (type 3 in Table 1) is nearly 3× lower than previous designs (17) (type 0), with a resonant frequency nearly 5× greater, resulting in up to 14-fold sensitivity improvements. Moreover, frequency noise decreases as oscillation amplitude increases, until Duffing-type mechanical nonlinearity

---

Significance

Naturally occurring and engineered nanoparticles (e.g., exosomes, viruses, protein aggregates, and self-assembled nanostructures) have size- and concentration-dependent functionality, yet existing characterization methods in solution are limited for diameters below ~50 nm. In this study, we developed a nanomechanical resonator that can directly measure the mass of individual nanoparticles down to 10 nm with single-attogram (10^{-18} g) precision, enabling access to previously difficult-to-characterize natural and synthetic nanoparticles.

ENGINEERING

BIOPHYSICS AND COMPUTATIONAL BIOLOGY

Table 1. Dimensions and theoretically calculated properties of the suspended nanochannel resonators

Type	Length, μm	Thickness, μm	Width, μm	Channel height, nm	Channel width, μm	Resonant frequency, MHz	Stiffness, N/m	Mass, pg	Sensitivity, mHz/ag	δm_{th} (ag)
Type 0	50	1	10	400	2	0.589	3.5	1,059	−1.15	2.7
Type 1	37.5	1	7.5	400	1	1.03	6.3	615	−3.47	1.2
Type 2	27	1	7.5	400	1	1.99	16.9	443	−9.3	0.5
Type 3	22.5	1	7.5	400	1	2.87	29.1	369	−16.1	0.3

Properties were calculated assuming the cantilevers are filled with water. The thermomechanical limit of mass resolution (δm_{th}) is the Allan deviation of thermal energy-induced frequency fluctuations of the cantilever motion (28, 29) at gate time of 1 ms, when the cantilever is driven at the onset of mechanical nonlinearity (21) (*SI Appendix*, sections 3 and 4).

is observed (24). To reach optimal oscillation amplitudes, we used piezoceramic actuators to drive the cantilevers (Fig. 1*A*). Driving cantilevers beyond their linear range caused spring stiffening, which was indicated by a right shift of the open-loop frequency response curves (Fig. 1*B*). In this work, all resonators were driven at their onsets of nonlinearity to achieve the best frequency stability. It was not possible to drive resonators into this regime with the electrostatic actuation that was used in the previous systems (15, 17).

In the new SNR system (*SI Appendix*, Fig. S1), an optical lever setup similar to one previously described (17) detects the cantilever's motion. The cantilever displacement signal acquired from a photodetector is phase-shifted via an adjustable delay on a field-programmable gate array (FPGA) and then amplified and fed back to a high-current amplifier driving a piezoceramic actuator. In the vicinity of the resonant frequency, intrinsic thermomechanical motion of the cantilever is the dominant source of noise on the photodetector output (*SI Appendix*, Fig. S2). The frequency of the oscillation is measured on the FPGA by digitally mixing the cantilever position signal down to 1 kHz and period counting using a 100-MHz clock.

To characterize the noise present in the frequency measurements of SNRs, we measured the oscillation frequency noise for different cantilevers (*SI Appendix*, Table S1) filled with ultrapure deionized water. We calculated the Allan deviations (25) (*Methods*) as a function of averaging (gate) times as shown in Fig. 2*A*, which is a common metric for oscillator noise. The Allan deviation of the overall oscillator system ranges from 4 to 8 parts per billion (ppb) at room temperature (without temperature control) using measurement rates of 5–1,000 Hz, which is the frequency range of interest for higher throughput. For type 2 and 3 cantilevers, this noise magnitude is equivalent to less than 1 ag (10^{-21} kg or 600 kilodaltons), which is demonstrated in Fig. 2*B* as mass-equivalent Allan deviation. The increasing noise at low gate times for type 0 and 1 cantilevers corresponds to white frequency noise, the flat region at the center for all cantilever types corresponds to the flicker (1/f) frequency noise and the ramp in the higher averaging durations corresponds to Brownian frequency noise and long-term frequency drift of the oscillators (26, 27).

To quantify the potential for further reductions in the noise level, we calculated the ultimate limit of frequency stability imposed by intrinsic thermomechanical fluctuations (28, 29) (*SI Appendix*, sections 3 and 4) for resonators driven at their onset of nonlinearity (21) (dashed lines in gray region of Fig. 2*A*). Measured frequency stability values at 1-ms gate time are 1.8- to 3.4-fold
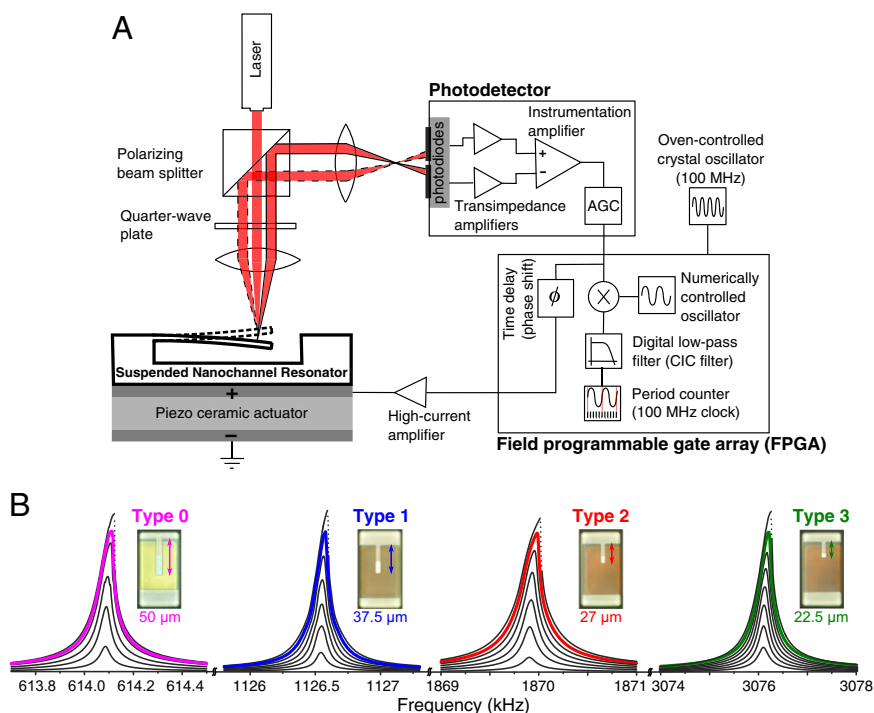

Fig. 1. Simplified schematic of the oscillator system with open-loop SNR frequency responses up to mechanical nonlinearity. (*A*) The SNR system (*SI Appendix*, Fig. S1) is a positive-feedback loop that keeps an SNR in oscillation. In the system, we used an optical lever to detect the cantilever deflection, a photodetector circuit to convert the laser deflection to a voltage signal, an FPGA to delay the photodetector signal and simultaneously measure the oscillation frequency, and an amplifier to drive the integrated piezoceramic actuator with the FPGA signal. The delay and the oscillation amplitude are controlled by the FPGA to achieve the minimum frequency noise. An oven-controlled crystal oscillator is used as the clock source for the FPGA. (*B*) Measured open-loop frequency responses of different types of SNRs used in this study (Table 1) for increasing drive levels, showing characteristic nonlinear behavior in the form of spring stiffening. The curves are normalized with respect to the peak amplitude at the onset of nonlinearity, which generates the minimum frequency noise in feedback. The frequency response curves at the onset of nonlinearity for each type are indicated as thicker, colored curves. (Insets) Optical micrographs of the cantilevers in the vacuum cavity with their lengths indicated below. Different types of cantilevers are color-coded, and the same color codes are used in Fig. 2.
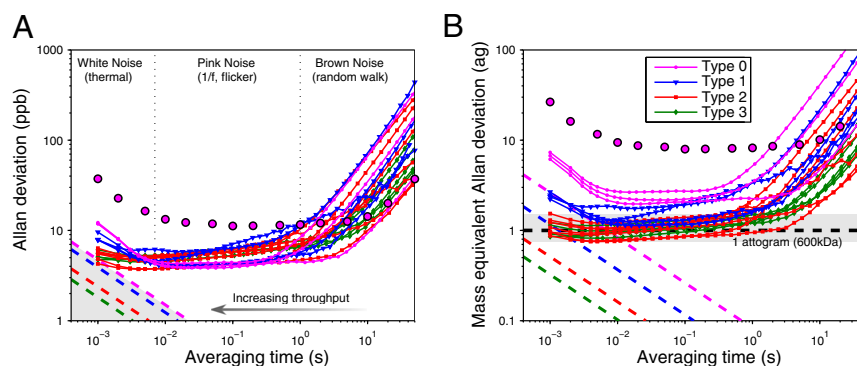
Fig. 2. Frequency noise and mass resolution of 20 different SNRs. (*A*) Frequency noise of each SNR, quantified as the Allan deviation and normalized by the mean frequency, is plotted as a function of averaging (gate) time. Ultimate noise limits imposed by thermal energy due to nonzero ambient temperature (*SI Appendix*, section 4) are shown as colored dashed lines in the lower left corner, and decrease as 1/(averaging time)$^{1/2}$. All lines are color-coded as in Fig. 1*B* with respect to the corresponding device types given in Table 1. Bigger pink circles show the Allan deviation of a type 0 cantilever as reported in ref. 17, which at 1-ms averaging time is more than 10× what we achieved in this work. The predominant noise mechanisms in the corresponding range of averaging times are indicated at the top and approximately delineated by thin dotted lines. (*B*) Mass resolution of each SNR, defined as the mass equivalent Allan deviation, is plotted as a function of the averaging time. Type 2 and 3 devices show typical mass resolutions of 0.75–1.5 ag (shaded region) from 1 to 200 ms averaging time. Colored dashed lines show the mass resolution limited by the thermal energy for corresponding type of cantilevers with matching color code. Measured mass sensitivities given in *SI Appendix*, Table S1 are used to convert the frequency noise in Fig. 2*A* to mass. For calculating the theoretical limits of mass resolution due to thermal energy, calculated mass sensitivities listed in Table 1 are used.

above the thermomechanical noise limits. For shorter (<10 to <1 ms) gate times, noise from the photodetector becomes the dominant factor (*SI Appendix*, Fig. S3), which sets a lower bound on the particle transit time and hence an upper bound on the throughput of the device. With further improvement of the detection system, it may be possible to achieve a 10-fold improvement in the throughput without sacrificing mass resolution (*SI Appendix*, section 3).

After we achieved mass sensitivities exceeding 16 mHz/ag and reduced frequency noise to 4 ppb, we focused on optimizing our peak detection scheme. We used the characteristic shape of a peak (30), determined by the flow path and the transit time of the particle, in a bank of matched filters for detecting the characteristic frequency modulation signal due to a particle transit with the maximum signal-to-noise ratio (31). The mass equivalent Allan deviation of type 2 and 3 devices is between 0.75 and 1.5 ag (gray region in Fig. 2*B*), which enables 3σ detection limits lower than 5 ag or 3 MDa (*SI Appendix*, Figs. S4 and S5).

Results

Mixture of Gold Nanoparticles. Mass distribution is an important measure of nanoparticle populations. We first demonstrated the mass resolution of our system by weighing a mixture of 10-, 15-, and 20-nm gold nanoparticles. Before analyzing the mixture, we calibrated the mass sensitivity (Hz/kg) of the resonator using size-calibrated gold nanoparticles (*SI Appendix*, Fig. S6). In a 97-min experiment, we measured more than 29,000 individual particles in the mixture (Fig. 3 *A* and *B*). The results show three distinct well-separated populations (Fig. 3*C*) ~9.1, 28.1, and 73.4 ag. Assuming all particles are spherical and uniformly dense, the mean sizes of the three populations are estimated to be 9.9, 14.4, and 19.7 nm, which agree well with the manufacturer specifications of 9.9, 14.3, and 20.4 nm (Fig. 3*D*). The coefficients of variation in diameter for each population were 7.4%, 5.3%, and 4.9%, respectively, compared with the datasheet values of <8% for 15- and 20-nm gold nanoparticles. Additionally, we compared our results to DLS measurements (*SI Appendix*, Table S2), which could not resolve the three populations separately in the gold nanoparticle mixture. We also tested the dynamic range of the SNRs by successfully weighing larger particles (150-, 200-, and

220-nm polystyrene beads) using the same operating, detection, and estimation conditions (*SI Appendix*, Fig. S7).

In addition to mass distribution, concentration is also a key parameter of nanoparticle suspensions. The SNR can provide a direct measure of nanoparticle concentration because the detection and estimation algorithm estimates the transit time of each particle (Fig. 3*B*) and the dimensions of the buried microfluidic channel are known. Based on the measurement shown in Fig. 3, the concentrations of 10-, 15-, and 20-nm gold nanoparticles in the mixture are 5.4×10^9, 3.6×10^9, and 3.7×10^9 particles per milliliter, respectively (see *SI Appendix*, section 9, for error analysis), which are comparable with the concentrations obtained from the particle datasheets (5.7×10^9, 3.1×10^9, and 3.9×10^9 particles per milliliter).

Heterogeneity of Exosomes from Different Cell Types. To demonstrate the capability of the SNRs to characterize relevant biological samples, we used exosomes, which are cell-derived vesicles present in the extracellular fluids that mediate intercellular communication via the exchange of proteins and genetic material (32, 33). Although there is immense scientific and clinical interest, detection and characterization of exosomes remain challenging. Purified exosomes from in vitro and clinical samples alike are heterogeneous because their size and density ranges from 30 to 100 nm and 1.13 to 1.19 g/cm^3, respectively (22), which translates into 2–100 ag buoyant mass in water. Moreover, exosomes from a mixed population of cells, i.e., normal vs. diseased cells, theoretically can differ in their cargo content, which in turn may alter their mass, size, and/or density. Optical methods such as DLS analysis can give comparative information about their mean size (*SI Appendix*, Table S3), but the heterogeneity and distribution shape of the populations, which may reflect differences in their biological functions, are difficult to measure. Therefore, we weighed exosomes that were produced by 3T3-J2 fibroblasts and primary hepatocytes, two inherently different cell types, which when cocultured have been shown to engage in both physical and molecular cell–cell interactions (34, 35). The buoyant mass distributions of exosomes derived from fibroblast and hepatocyte cells reveal clear differences in heterogeneity (Fig. 4). The relative broadness in buoyant mass of the fibroblast exosomes suggests the presence of either a larger or denser subpopulation compared with the exosomes derived
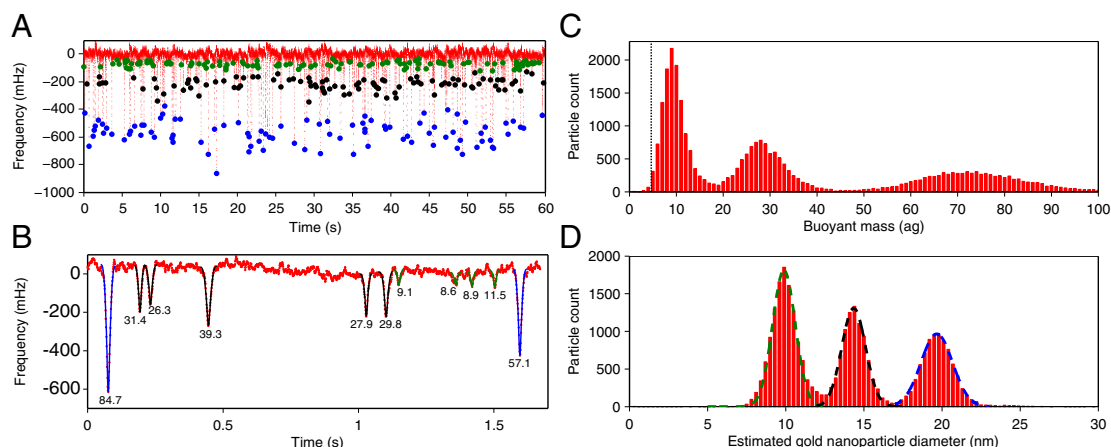
Fig. 3. Buoyant mass measurements of a mixture of 10-, 15-, and 20-nm gold nanoparticles. (*A*) An arbitrary 60-s oscillation frequency measurement around the resonant frequency of the SNR during a 97-min-long experiment. Data were acquired at 1 kHz and filtered with a five-point second-order Savitzky–Golay filter and a second-order IIR high-pass filter with 1-Hz cutoff frequency. Particles detected by the bank of matched filters (*Methods*) are marked with circles color-coded with respect to their buoyant masses (green for <18 ag, blue for >44 ag, black for in between). (*B*) Each detected peak is further analyzed for estimating the buoyant mass and the transit time of the particle by fitting it to the expected peak shape for a particle transiting the cantilever with a constant velocity. Estimated buoyant mass value for each detected particle is indicated underneath the peak along with the estimated color-coded peak shape. (*C*) Buoyant mass histogram of 29,000 particles detected during the experiment. The thin dotted line at ~5 ag is the limit of mass detection in the experiment. (*D*) Diameter histogram, calculated assuming particles are uniform spheres of density 19.3 g/cm³. Dashed lines show fits to Gaussians. Particle peaks shown in *A* and *B* belong to the corresponding populations in *D* with the matching color. The fits indicate mean sizes of 9.9, 14.4, and 19.7 nm with coefficients of variation of 7.4%, 5.3%, and 4.9%, respectively.

from hepatocytes, which shows less dispersion with a 35% co-efficient of variation in mass and a median of 8.6 ag; this translates into a median diameter of 48 nm (Fig. 4, *Inset*), assuming a spherical shape and uniform exosome density of 1.16 g/mL (see *SI Appendix*, Fig. S9 for the effect of density assumption on size). We observe a rapid increase in the exosome concentrations in both populations with decreasing buoyant mass from 20 to 10 ag. Similar size distributions have been measured using transmission electron microscopy (TEM) previously (36) on other types of exosome samples. It is worth noting that the shape of the distribution below ~7–8 ag is uncertain, because what we observe in this region is predominantly defined by the detection probability (*SI Appendix*, Fig. S8C). We repeated the experiments using a different cantilever on the same samples as well as on a second

batch of purified fibroblast and hepatocyte exosomes. The results of the repeated runs (*SI Appendix*, Fig. S10) suggest the same difference in population heterogeneity presented in Fig. 4. We determined the concentrations of the purified stocks as being 3.3×10^{12} and 1.3×10^{12} particles per milliliter for fibroblast and hepatocyte exosomes, respectively, demonstrating that this technique can be used to quantify yields of exosome purifications as well.

Yield of DNA Origami–Gold Nanoparticle Assemblies. To further demonstrate the absolute concentration measurement capability of the SNR, we characterized the binding efficiency of func-tionalized gold nanoparticles to DNA origami structures. DNA nanotechnology has great promise for developing precise nano-structures, such as scaffolds for molecular nanodevices (37). However, practical and accurate methods are required for assessing the yield of complex DNA structures. We designed DNA origami structures as scaffolds with two and three binding sites for gold nanoparticles (*SI Appendix*, Figs. S11 and S12) and validated the binding of gold nanoparticles to DNA origami by gel electrophoresis and atomic force microscopy (AFM) (*SI Appendix*, Fig. S13). We weighed ssDNA-modified 15-nm gold nanoparticle binding agents with the SNR and observed that ~13% of the DNA-modified gold nanoparticle population were not singles (as defined as weighing more than 45 ag), with only 3.3% of the population being above 75 ag (9×10^7 particles per milliliter). This population results from two or more particles that agglomerated due to nonspecific binding of the modified DNA. We then weighed the DNA origami structures with two binding sites with modified gold nano-particles. The abundance of the nonsingles increased to 32%, with 9% of this fraction weighing above 75 ag (1.3×10^8 particles per milliliter). This increase in the nonsingles indi-cates the successful binding of the gold nanoparticles to the DNA origami structure. Finally, we weighed the DNA origami structures with three binding sites with modified gold nano-particles and, as expected, observed a broader distribution of particles compared with the previous samples. We calculated the concentration of the particles that are heavier than 75 ag
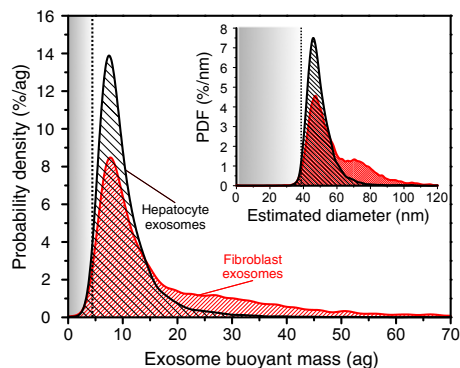

Fig. 4. Buoyant mass measurements of exosomes derived from different cell types. Buoyant mass distributions (kernel density estimates) of fibro-blast-derived (red) and hepatocyte-derived (black) exosomal vesicles. Some 7,100 fibroblast exosomes and 9,600 hepatocyte exosomes are weighed us-ing an SNR in 65-min and 76-min experiments, respectively. The limit of detection is depicted with a vertical dotted line close to 5 ag. (*Inset*) Esti-mation of exosome diameter by assuming a spherical shape and a constant exosome density of 1.16 g/mL throughout the populations. The vertical dashed line indicates the corresponding limit of mass detection as 39 nm.
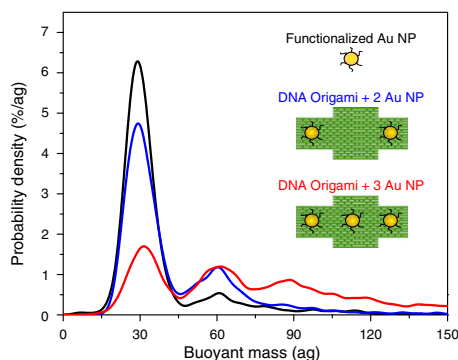
Fig. 5. Buoyant mass measurements of DNA origami–gold nanoparticle assemblies. Buoyant mass distributions (kernel density estimates) of functionalized 15-nm gold nanoparticles (Au NP) with ssDNA (black) mixed with DNA origami structures with two binding sites (blue) and DNA origami structures with three binding sites (red).

as 4.1×10^8 particles per milliliter, which constitute about 47% of the population. The resulting buoyant mass distributions for the three sample populations are shown in Fig. 5. Although gel electrophoresis can provide similar distributions, it cannot provide a measure of absolute concentration. Because the flow rate through the SNR in this experiment was ~3 nL/h, we envision that SNRs could ultimately be used as a real-time tool to quantify nanostructure assemblies.

Outlook

The demonstrations presented in this paper suggest that the SNR can be a valuable complement to the existing methods for characterizing nanoparticles in solution. High-precision mass measurement could allow us to identify signatures of pathology in blood plasma regardless of the molecular properties of the target. For example, glioblastoma cells are known to secrete microvesicles (50–500 nm) that have been implicated in angiogenesis (32). However, assessing if such nanoscale vesicles display a unique size or concentration signature has previously been extremely difficult. Combining volume measurements via resistive pulse sensing and buoyant mass measurements via the SNR at the level of individual nanoparticles would reveal their density, further increasing potential diagnostic power. For exosomes, measuring density would enable small particles with high amounts of cargo to be distinguished from large particles with limited cargo. Moreover, the SNR can potentially be used to discriminate between exosomes and larger extracellular microvesicles, which differ in size (38) and potentially differ in terms of their function. Because the contents of microvesicles and exosomes remain poorly characterized, multiparameter physical measurements together with molecular measurements could help elucidate their biological functions. In addition, future SNR implementations incorporating particle sorting and collection could allow purification and downstream analyses on a range of biological and synthetic nanoparticle populations. Such SNR implementations could be used for monitoring nanoparticle formation kinetics and ultimately for improving the techniques for engineering synthetic nanoparticles with desired properties.

Methods

SNR Fabrication. SNRs were manufactured by a previously described process (15, 17), which was performed at Innovative Micro Technology. The process enables each cantilever to freely oscillate in a dedicated vacuum cavity with an on-chip getter to maintain the high vacuum required for the high-Q operation. There are four fluidic ports drilled on the top glass wafer to access the two bypass channels (50 × 20 µm) separated 285 µm apart at each side of the cantilever. The U-shaped channel in the cantilever is connected to

these bigger bypass channels by 140-µm channels with the same cross-section that is in the cantilever.

System Operation. The displacement noise of the cantilever due to the thermal energy is amplified in a positive feedback loop to achieve a sustainable self-oscillation according to the Barkhausen criteria (39) at the instantaneous resonant frequency of the cantilever. The frequency of oscillation is measured by period counting at 100 MHz using a digital heterodyne mixer and a low-pass filter coded in the FPGA (*SI Appendix*, section 2). We use computer-controlled electronic pressure regulators connected to pressurized glass sample vials to control the flow in the bypass channels and in the SNR.

Allan Deviation. The Allan deviation, $\sigma_A(\tau)$, of the oscillation frequency of an oscillator in a time period of τ is defined as in ref. 40:

$$\sigma_A(\tau) = \sqrt{\sigma_A^2(\tau)} \approx \sqrt{\frac{1}{2(N-1)} \sum_{k=2}^{N} \left(\frac{\overline{f}_k - \overline{f}_{k-1}}{f_0}\right)^2},$$

where $\overline{f}_k$ is the time average of the frequency measurement in the kth time interval of τ within a total of N intervals, and f_0 is the mean oscillation frequency calculated over the entire duration of the noise measurement. In other words, the Allan deviation is calculated by averaging subsequent sections of the normalized frequency data of length τ, and then taking the difference between the means of contiguous segments.

Peak Detection and Estimation. Measured frequency data by the FPGA is sent to a control computer in real time via Ethernet and is recorded by the computer. The recorded data are analyzed afterward using postprocessing code in MatLab. First, the mean of the data are subtracted and the result is high-pass filtered by a second-order IIR notch filter with 1-Hz cutoff frequency. Next, the data are filtered with a bank of matched filters (*SI Appendix*, Fig. S4) with coefficients having a shape of a frequency peak (30) resulting from a particle passing through the SNR. The widths of the filters in the bank are adjusted to span the possible transit times of the particles for that particular experiment, and their amplitudes are normalized to their norms. At each point in time, the maximum among the matched filter outputs is selected and normalized to the corresponding filter norm to set the overall gain for a peak as unity. Finally, the peak positions in time that are above the limit of detection are determined (Fig. 3A), and the detected peaks are analyzed individually (Fig. 3B). The baseline and the peak shape are fit around each frequency minimum on the high-pass filtered frequency data using a least-squares fit algorithm.

Calibration. The mass sensitivity of a cantilever is determined by running a population of gold nanoparticles [RM 8012 by National Institute of Standards and Technology (NIST)] as a reference material before the actual experiment. Cantilever sensitivity is calculated using the mean particle diameter (26.5 nm), which was estimated by AFM, SEM, and TEM measurements as described in the reference material datasheet. The resulting mass histogram and size estimation are given in *SI Appendix*, Fig. S6.

Gold Nanoparticle Measurements. A type 2 device (11M in *SI Appendix*, Table S1) was used to weigh the nanoparticle mixture comprised of 10- (NIST RM 8011), 15-, and 20-nm (EMGC15 and EMGC20 from BBI Solutions) gold. Samples were diluted in filtered (0.22 µm) deionized water 300, 150, and 60 times, respectively. We mixed 0.5 mL of diluted 10-, 15-, and 20-nm gold particles together before the experiment, which increased the total dilutions to 900, 450, and 180 times, respectively. The accuracy of the concentration estimation increases with the signal-to-noise ratio of the particles in the sample (*SI Appendix*, section 9). Therefore, we calculated flow rate in the SNR using the 20-nm particle signal, which has the highest signal-to-noise ratio in the mixture.

Functionalization of Gold Nanoparticles with DNA. DNA-modified gold nanoparticles (*SI Appendix*, Fig. S11) were prepared using previous reports (41). Gold nanoparticles (15 nm; Ted Pella Inc.) were stabilized with Bis(p-sulfonatophenyl)phenylphosphine dihydrate dipotassium salt (BSPP). BSPP (18 mg) was dissolved in gold nanoparticle solution (25 mL), and the mixture was stirred overnight at room temperature. Sodium chloride was added slowly to the solution with stirring until the color changed from red to light purple. The resulting solution was centrifuged at 966 × g for 30 min. The supernatant was carefully removed and the gold nanoparticles were dispersed in 0.5 mL BSPP (2.5 mM) with 0.5 mL methanol. The solution was centrifuged at 21,130 × g for 30 min. The supernatant was removed and gold nanoparticles

were dispersed again in 0.25 mL BSPP (2.5 mM). Next, 80 μL T_{28}-SH DNA (100 μM) was activated with 20 μL Tris-(2-carboxyethyl)phosphine hydrochloride (100 mM). The activated thiol-modified DNA was purified using a NAP-5 column (GE Healthcare). The phosphinated gold nanoparticles and thiol-modified DNA (gold nanoparticle:DNA = 1:200) were incubated in 1 M Tris, 0.9 M boric acid, 0.01 M EDTA (pH 8.0) containing NaCl (50 mM) for 15 h at room temperature, which enabled the stabilization of gold nanoparticles under high-salt conditions.

Preparation of the DNA Origami. The molar ratio of 1:5 between M13mp18 viral ssDNA and staple strands was used. DNA origami was assembled in 40 mM Tris, 20 mM acetic acid, 2 mM EDTA (pH 8.0) buffer (1×) containing magnesium acetate (12.5 mM) by annealing from 95 °C for 5 min to 60 °C over 35 min, and cooled further to 15 °C over 135 min. The annealing product was purified using spin filtration (MWCO, 100 K; Millipore) to remove extra staple strands. The constructed DNA origami was examined by AFM (*SI Appendix*, Fig. S12). DNA origami structures with two and three binding sites were prepared by substituting original staple strands for hook staple strands. Purified DNA origami was mixed with thiol-modified gold nanoparticles and annealed from 37 °C to 15 °C over 110 min. Finally, we examined the products purified by agarose gel by AFM (*SI Appendix*, Fig. S13).

Exosome Experiments. Exosomes were purified from supernatants of 3T3-J2 fibroblasts cultured at 37 °C, 5% CO_2 in DMEM with high glucose, 10% (vol/vol) exosome-depleted FBS, and 1% penicillin–streptomycin. 3T3-J2 fibroblasts were cultured until ~60% confluency at which point media was replaced with exosome-depleted fibroblast media. After 48 h, 3T3-J2 media was collected and centrifuged at 1,800 × g for 10 min to remove cells. Hepatocytes exosomes were obtained from primary rat hepatocytes cultured in DMEM with

high glucose, 10% (vol/vol) exosome-depleted FBS, 0.5 U/mL insulin, 7 ng/mL glucagon, 7.5 μg/mL hydrocortisone, and 1% penicillin–streptomycin. Twelve million hepatocytes were seeded in T150 flasks for 3 h to obtain ~80% confluency. After 3 h, media was collected, centrifuged at 3,000 rpm for 10 min to remove cells, and replaced with fresh exosome-depleted hepatocyte media. Following an additional 24 h of culture, hepatocyte media was again collected, centrifuged at 3,000 rpm for 10 min to remove cells, and pooled with hepatocyte media collected the previous day. Exosomes were purified from media using differential centrifugation. Briefly, media was centrifuged at 10,000 × g for 1 h and subsequently processed through a 0.22-μm filter. A crude exosome pellet was obtained by ultracentrifugation at 100,000 × g for 3 h at 4 °C and resuspended in 0.22 μm filtered PBS. Washed exosomes were again pelleted at 100,000 × g for 2 h at 4 °C and resuspended in 150 μL filtered PBS. To remove any copurified protein complexes, exosomes were further purified by size-exclusion chromatography over a Sepharose CL-4B resin column (GE Healthcare). Exosome containing fractions, as detected by DLS analysis, were pooled and pelleted at 100,000 × g for 2 h at 4 °C. Finally, purified exosomes were resuspended in 100 μL filtered PBS for further analysis. We diluted the prepared fibroblast exosomes 500× and hepatocyte exosomes 200× in 0.22 μm filtered 1× PBS before running the populations through a type 3 SNR (see 7B in *SI Appendix*, Table S1).

1. Peer D, et al. (2007) Nanocarriers as an emerging platform for cancer therapy. *Nat Nanotechnol* 2(12):751–760.
2. Morachis JM, Mahmoud EA, Almutairi A (2012) Physical and chemical strategies for therapeutic delivery by using polymeric nanoparticles. *Pharmacol Rev* 64(3):505–519.
3. Chi EY, Krishnan S, Randolph TW, Carpenter JF (2003) Physical stability of proteins in aqueous solution: Mechanism and driving forces in nonnative protein aggregation. *Pharm Res* 20(9):1325–1336.
4. Sauerborn M, Brinks V, Jiskoot W, Schellekens H (2010) Immunological mechanism underlying the immune response to recombinant human protein therapeutics. *Trends Pharmacol Sci* 31(2):53–59.
5. Théry C, Ostrowski M, Segura E (2009) Membrane vesicles as conveyors of immune responses. *Nat Rev Immunol* 9(8):581–593.
6. Anderson W, Kozak D, Coleman VA, Jämting ÅK, Trau M (2013) A comparative study of submicron particle size platforms: Accuracy, precision and resolution analysis of polydisperse particle size distributions. *J Colloid Interface Sci* 405:322–330.
7. Lange H (1995) Comparative test of methods to determine particle size and particle size distribution in the submicron range. *Part Part Syst Charact* 12(3):148–157.
8. Mahl D, Diendorf J, Meyer-Zaika W, Epple M (2011) Possibilities and limitations of different analytical methods for the size determination of a bimodal dispersion of metallic nanoparticles. *Colloids Surf Physicochem Eng Asp* 377(1-3):386–392.
9. Fraikin J-L, Teesalu T, McKenney CM, Ruoslahti E, Cleland AN (2011) A high-throughput label-free nanoparticle analyser. *Nat Nanotechnol* 6(5):308–313.
10. Roberts GS, et al. (2010) Tunable nano/micropores for particle detection and discrimination: Scanning ion occlusion spectroscopy. *Small* 6(23):2653–2658.
11. Chaste J, et al. (2012) A nanomechanical mass sensor with yoctogram resolution. *Nat Nanotechnol* 7(5):301–304.
12. Jensen K, Kim K, Zettl A (2008) An atomic-resolution nanomechanical mass sensor. *Nat Nanotechnol* 3(9):533–537.
13. Naik AK, Hanay MS, Hiebert WK, Feng XL, Roukes ML (2009) Towards single-molecule nanomechanical mass spectrometry. *Nat Nanotechnol* 4(7):445–450.
14. Hanay MS, et al. (2012) Single-protein nanomechanical mass spectrometry in real time. *Nat Nanotechnol* 7(9):602–608.
15. Burg TP, et al. (2007) Weighing of biomolecules, single cells and single nanoparticles in fluid. *Nature* 446(7139):1066–1069.
16. Barton RA, et al. (2010) Fabrication of a nanomechanical mass sensor containing a nanofluidic channel. *Nano Lett* 10(6):2058–2063.
17. Lee J, Shen W, Payer K, Burg TP, Manalis SR (2010) Toward attogram mass measurements in solution with suspended nanochannel resonators. *Nano Lett* 10(7):2537–2542.
18. Yang YT, Callegari C, Feng XL, Ekinci KL, Roukes ML (2006) Zeptogram-scale nanomechanical mass sensing. *Nano Lett* 6(4):583–586.
19. Ekinci KL, Roukes ML (2005) Electromechanical transducers at the nanoscale: Actuation and sensing of motion in nanoelectromechanical systems (NEMS). *Small* 1(8-9):786–797.
20. Feng XL, White CJ, Hajimiri A, Roukes ML (2008) A self-sustaining ultrahigh-frequency nanoelectromechanical oscillator. *Nat Nanotechnol* 3(6):342–346.
21. Arlett JL, Roukes ML (2010) Ultimate and practical limits of fluid-based mass detection with suspended microchannel resonators. *J Appl Phys* 108(8):084701.
22. Théry C, Zitvogel L, Amigorena S (2002) Exosomes: Composition, biogenesis and function. *Nat Rev Immunol* 2(8):569–579.
23. Ekinci KL, Yang YT, Roukes ML (2004) Ultimate limits to inertial mass sensing based upon nanoelectromechanical systems. *J Appl Phys* 95(5):2682–2689.
24. Greywall DS, Yurke B, Busch PA, Pargellis AN, Willett RL (1994) Evading amplifier noise in nonlinear oscillators. *Phys Rev Lett* 72(19):2992–2995.
25. Rutman J, Walls FL (1991) Characterization of frequency stability in precision frequency sources. *Proc IEEE* 79(6):952–960.
26. Leeson D (1966) A simple model of feedback oscillator noise spectrum. *Proc IEEE* 54(2):329–330.
27. Rubiola E (2009) *Phase Noise and Frequency Stability in Oscillators* (Cambridge Univ Press, Cambridge, UK).
28. Albrecht TR, Grütter P, Horne D, Rugar D (1991) Frequency modulation detection using high-Q cantilevers for enhanced force microscope sensitivity. *J Appl Phys* 69(2):668–673.
29. Cleland AN, Roukes ML (2002) Noise processes in nanomechanical resonators. *J Appl Phys* 92(5):2758–2769.
30. Dohn S, Svendsen W, Boisen A, Hansen O (2007) Mass and position determination of attached particles on cantilever based mass sensors. *Rev Sci Instrum* 78(10):103303–103333.
31. Hippenstiel RD (2002) *Detection Theory: Applications and Digital Signal Processing* (CRC, Boca Raton, FL).
32. Skog J, et al. (2008) Glioblastoma microvesicles transport RNA and proteins that promote tumour growth and provide diagnostic biomarkers. *Nat Cell Biol* 10(12):1470–1476.
33. Peinado H, et al. (2012) Melanoma exosomes educate bone marrow progenitor cells toward a pro-metastatic phenotype through MET. *Nat Med* 18(6):883–891.
34. Hui EE, Bhatia SN (2007) Micromechanical control of cell-cell interactions. *Proc Natl Acad Sci USA* 104(14):5722–5726.
35. Khetani SR, Bhatia SN (2008) Microscale culture of human liver cells for drug development. *Nat Biotechnol* 26(1):120–126.
36. van der Pol E, et al. (2010) Optical and non-optical methods for detection and characterization of microparticles and exosomes. *J Thromb Haemost* 8(12):2596–2607.
37. Douglas SM, Bachelet I, Church GM (2012) A logic-gated nanorobot for targeted transport of molecular payloads. *Science* 335(6070):831–834.
38. Simons M, Raposo G (2009) Exosomes—vesicular carriers for intercellular communication. *Curr Opin Cell Biol* 21(4):575–581.
39. Hajimiri A, Lee TH (1999) *The Design of Low Noise Oscillators* (Kluwer Academic, Boston).
40. Barnes J, et al. (1971) Characterization of frequency stability. *IEEE Trans Instrum Meas* 20(2):105–120.
41. Sharma J, et al. (2008) Toward reliable gold nanoparticle patterning on self-assembled DNA nanoscaffold. *J Am Chem Soc* 130(25):7820–7821.